SH-wave seismic reflection at a landslide (Patigno, NW Italy) integrated with P-wave

E. Stucchi [1], A. Tognarelli[2], A. Ribolini[2]

[1]Earth Sciences Department, University of Milan, Italy
[2]Earth Sciences Department, University of Pisa, Italy

Abstract

The aim of this paper is to present the acquisition and processing up to the depth migrated section of an SH-wave reflection seismic profile. This experience is conducted on a deep-seated gravitational slope deformation located in the Northern Apennines in Italy. The SH-wave depth-migrated image in the investigated area provides a detailed description of the small reactivation slip surfaces delineating minor landslides at shallow depths, which are responsible for the major damages observed. These results are integrated with a recently acquired P-wave seismic reflection profile investigating the same slope and delineating the highly deformed layer at depth, liable for the deep-seated gravitational slope deformation. The combined use of P-waves and SH-waves allows to gain a deeper knowledge of the landslide internal setting that is necessary to mitigate the risk associated with the mass movement.

1. Introduction

The widespread use of the P-wave reflection survey in seismic exploration is motivated by the ease with which the P-wave seismic data can be acquired and processed with respect to S-wave data, and by the possibility of obtaining seismic sections with high signal-to-noise ratio (S/N) that provide clear and detailed images of the subsurface. However, when only P-waves are considered, the physical properties characterizing their propagation can sometimes limit the objectives of seismic investigation. This is the case, for instance, when a discrimination between the presence of fluids and of different lithologies is desired (Castagna and Backus, 1993), or when the resolution required cannot be achieved with the wavelengths characterizing P-wave propagation (Johnson and Clark 1992; Pugin et al. 2004; Guy, 2006; Pugin et al. 2006; Polom et al. 2013). From a theoretical point of view, S-wave surveys can overcome these limitations, explaining the efforts for their increasing usage. The preferred

choice for S-wave investigation is to use SH-waves which, owing to the horizontal displacement of the particle motion, do not convert to P- or SV-waves in case of horizontal reflecting boundaries (Binbin et al., 2015). However, in addition to geophones measuring the horizontal velocity of particle motion, seismic sources need to be built that generate high SH-wave energy in the cross-line direction, but little energy along the seismic line in order to limit the unwanted P- or P-SV-wave modes. Furthermore, all the acquisition survey parameters must be re-designed according to the different propagation characteristics of the SH-waves (Pugin et al., 2004; Guy, 2006; Pugin et al., 2006).

In the literature there is an increasing interest in the SH-wave reflection seismic method applied to investigate the near-surface. Studies related to unconsolidated alluvial sediments and groundwater reservoirs (Young and Hoyos, 2001; Pugin et al., 2009; Haines and Ellefsen, 2010), to shallow subsurface structures and faults (Bexfield 2006, Beilecke et al. 2016) and to geo-hazards and earthquake hazards (Guy et al., 2003; Inazaki, 2004; Ghose et al., 2013; Krawczyk et al., 2013; Carvalho et al., 2016; Wadas et al., 2016) have been performed successfully. In the near-surface investigation a crucial issue is the higher resolution that can be achieved with the SH-waves over the P-waves because of the shorter wavelength featuring SH-wave propagation (Johnson and Clark 1992; Inazaki, 2004; Pugin et al., 2013; Beilecke et al. 2016; Wadas et al, 2016). Unfortunately, this higher resolution is usually accompanied by a reduced depth of investigation caused by the stronger attenuation to which SH-waves are submitted with respect to P-waves, attenuation which lowers the signal-to-noise ratio for targets at the same depth. Therefore, a combined use of SH- and P-wave methods is a possible strategy to overcome the issue related to resolution and depth-of-investigation. Researches where the P- and SH-wave reflection methodologies are used jointly to exploit the advantages that can be obtained by both techniques are reported, for example, in Woolery and Street, 2002; Pugin et al. 2004; Bexfield et al., 2006; Guy 2006; Pugin et al. 2009; Wiyono et al. 2013; Petronio et al., 2016; to mention just a few (even if in the last case that deals with a landslide, the SH-wave profile has not been processed). The joint use of the two methods is particularly interesting in the case of investigations concerning slip surfaces in large active landslides. Indeed, both the main sliding surface at depth and the shallow layers responsible for the quick reactivation movements need to be mapped.

In recent years, shallow reflection seismic has been employed to map the discontinuity associated with the deep sliding surface that characterizes large landslides. Only a few examples of application of this technique for a better delineation of the mass movement phenomenon can be found in the literature (Bichler et al. 2004; Stucchi and Mazzotti 2009; Apuani et al. 2012; Malehmir et al., 2013; Stucchi et al., 2014). One of the main reasons for

the lack of applications in this context is likely to be the low S/N ratio generally affecting the shallow seismic reflection data acquired in such complex near-surface environments (Jongmans and Garambois, 2007). Despite these difficulties, the constraint of deep and shallow discontinuities in a large landslide, the Patigno landslide (Federici et al., 2002) located in the upper basin of the Magra River in the Northern Apennines, Italy, was achieved (Tognarelli et al., 2015). Here, a P-wave reflection study (Stucchi et al., 2014) was effective to image the deepest discontinuity of the slope deformation at around 40-50 m depth, but unable to provide any geometrical description of the shallower layers at depths above 20 m. In this paper the work done by Tognarelli et al. (2015) is expanded in order to better describe some crucial processing steps and the joint interpretation of the P- and SH-wave seismic sections in depth.

2. Geological and geomorphological setting

The Patigno landslide is a large mass movement in the Northern Apennines (Italy) (Fig. 1 a), developing between 950 m and 550 m a.s.l. for a total length of 2,500 m and with a mean slope of about 10° (Fig. 1 b). The movement covers a total area of about 1.360 km^2 involving limestone with interbedding of grey-black argillites (Argille e Calcari Formation), limestone-marly turbidites (Calcari del Groppo del Vescovo Formation), and pelitic-siltitic turbidite (Arenarie di Ponte Bratica Formation). Limestones and olistolithes of serpentinite (Ottone S. Stefano Unit) flank the western side of the landslide.

The landslide experienced several active or dormant reactivations that dismantled the main body in many minor landslides, one of the largest and most active being the one located near the S. Lorenzo church (Fig. 1 b, Fig. 2a) to the south of the Patigno village. Indeed, boreholes located in this area (Fig. 2a) provided SE displacement of up to 3.5 cm at a depth of 12-19 m every six months, and up to 0.3-0.4 cm at a depth of 20-40 m (Federici et al., 2002; Stucchi et al., 2014) every six months. These displacements are consistent with borehole stratigraphy (Fig. 2b), which exhibits a shallow landslide body composed of boulders, gravel and coarse sand resting on highly fractured argillites and limestone with a weak geomechanical behavior, i.e. shear strength and cohesion that were qualitatively determined (Federici et al. 2002). The measured slow-rate displacements claimed for the existence of visco-plastic deformations in the deep layer (20-40 m of depth), according to a deep-seated slope gravitational deformation (Federici et al. 2002).

3. Acquisition and processing

Table 1 summarizes the acquisition parameters. Below we describe the parameters that are more peculiar to our SH-wave survey. The source was very similar to a see-saw that can be easily assembled and disassembled in the field. A swinging weight of 16 kg with a rope at the top of the see-saw was hung and left to drop, horizontally hitting a baseplate fixed by four nails on the ground. In order to generate SH-wave energy, the strike direction was orthogonal to the seismic profile, heading both NE-SW and SW-NE: two data sets with different polarization characteristics were acquired and then appropriately summed in the laboratory (reversing the data with SW-NE polarity) to increase the SH-wave S/N ratio. A vertical stack of 6 blows was applied for each source position and polarization. The source position distance was set at 1.5m.

Fig. 3 presents the acquisition scheme in detail. We used a cable layout consisting of 48 horizontal geophones at 10 Hz in an off-end configuration with receiver spacing of 0.75 m. The nominal maximum offset obtained is 41.25 m due to an in-line gap of 6 m. Every 7 source station the cable was rolled along downhill until we reached the last cable position at the damaged church (see also Fig. 2a); in this final spread position the data were also acquired for all the source stations inside the spread, in order to increase coverage. Total profile length is approximately 86 m in NW-SE direction, overlapping part of the previously acquired P-wave seismic line (Fig. 2a).

Fig. 4 (a,b) displays two raw blow gathers acquired with NE-SW and SW-NE strike directions respectively. The results of vertical stack and summation with polarity reversal are shown in Fig. 4c. The high level of coherent noise - mainly Love waves - contaminating the data and overwhelming the reflected signal is evident (Fig. 4c). Love waves constitute a particular type of surface waves characterized, like the Rayleigh waves, by high energy and dispersive behavior. The waves also have recording time and frequency band overlapping those of the desired signal, and for this reason their attenuation requires careful application of dedicated algorithms. The de-noising procedure tailored for the attenuation of the Love waves that we used consists of the following steps: eigenvalue filter, fk filter and band-pass filter, shown in the yellow boxes of the processing flowchart in Fig. 5. The different colors in the flowchart highlight the domain in which the processing algorithms were applied. As it can be observed, many steps were performed in the shot domain, since we found that tackling the various noises in this domain was more effective for their attenuation.

As concerns the Love waves, we need to resort to an accurate design of an eigenvalue filter to increase the S/N ratio at the pre-stack level. In detail, the eigenvalue filter was applied on

shot data where the main event corresponding to the Love waves was flattened by means of static shifts (horizon flattening). This allowed the filter to be more effective so that a limited number of eigenimages, those corresponding to the surface waves, needed to be subtracted (4 eigenimages). Figures 6a and 6b display a raw blow gather and the eigenvalue filtered gather, respectively. Fig. 6b shows clearly that most of the Love wave energy has been attenuated by the eigenvalue filter, even if some residual components still remain. These components are caused by minor misalignements and/or different shape of the wavelet at short and far offset characterizing the surface waves. A polygonal *f-k* filter was applied to remove this residual Love wave energy and its outcome is shown in Fig. 6c. The reflection around 250 ms, previously hidden at far offset by the Love waves, is now more evident; moreover, at shallower time and at short offsets some other weak events can also be appreciated after the application of the gain computed as the inverse of the envelope (Fig. 6d).

Refraction statics, computed as soon as the database of the acquisition geometry was built, were then applied. A two layer model was used to compute the refraction statics, by estimating the velocity of the first layer by means of the first arrivals of the short offset traces (V_0=150 m/s). The refractor offset we employed ranges from 9 m to 18 m, and the resulting model obtained by the generalized reciprocal method (GRM, Palmer 1981) is displayed in Fig. 7, with the reference datum set at 687 m a.s.l.. Only minor changes are observed in the refractor velocity, which varies in the range 175-240 m/s.

Velocity analysis was performed on supergathers formed by 5 adjacent CMPs to increase the S/N ratio, by computing the signal coherency along hyperbolic trajectories by means of the conventional semblance (C_S) (Neidell and Taner, 1971):

$$C_s = \frac{1}{M} \frac{\sum \left(\sum d_i \left(t_0 ; v_{\text{stack}} \right) \right)^2}{\sum \sum d_i^2 \left(t_0 ; v_{\text{stack}} \right)},$$

where M is the number of traces of the seismic data gather *d* and *T* is the width of the hyperbolic time window. This result was then refined by using the higher resolution complex matched functional (C_{CM}):

$$C_{cm} = \frac{1}{M} \frac{\sum \left| \sum \left(D_i ; t_0 , v_{\text{stack}} \right) \right|^2}{\sum \sum \left| \left(D_i ; t_0 , v_{\text{stack}} \right) \right|^2},$$

where *D* is the analytic (i.e. Hilbert transformed) data *d* filtered by the analytic Ricker wavelet at 30 Hz (Grandi et al., 2007, Tognarelli et al. 2013, Aleardi et al. 2016).

As an example, Fig. 8 shows a supergather (Fig. 8a) and the corresponding velocity spectra computed with the C_S and C_{CM} algorithms (Fig. 8 b,c respectively). The velocity panels clearly show high coherency values related to many events, and allow us to track the

reflection trend by picking the white dot points from CMP to CMP along the line (Fig. 8 b,c). The hyperbolic paths of the main reflections that we observed, each one indicated by an arrow, were drawn on the CMP supergather (red dashed lines in Fig. 8a) and their t_0 times were checked on the resulting stack section (red dots in Fig. 9b). A total of 20 gathers were considered for the velocity analysis. We built an initial velocity model picking the (t_0, V_{SH}) pairs on the C_S panels (Fig. 8b); this model was successively refined in its more relevant points, by using the higher resolution maps of the C_{CM} functional (Fig. 8c).

Besides the classical steps of NMO correction, residual statics computation and stack, the following post-stack de-noising operations were applied. The first is a time variant filter (TVF) with the bandwidth narrowing and moving to the lower frequency as the recording time increases. The filter parameters, estimated by means of spectral analysis, are listed in Fig. 5 and the stack section is shown in Fig. 9a. In this section the deeper reflections (250-350 ms) demonstrate good lateral continuity, while the coherency of the shallower ones is partially disrupted by residual noise. We thus applied a second de-noising step consisting of an *f-x* deconvolution, which helped to get rid of this noise and to better highlight the near-surface structures of the landslide (Fig. 9b).

The stacking velocity field obtained by the velocity analysis was depth-converted by the Dix equation and then smoothed. The resulting velocity field was used as input to the Kirchhoff post-stack depth migration, over-imposed to the same velocity field for a rough quality check (Fig. 10). The good S/N ratio that the depth migrated section exhibits up to 40-50 m (Fig. 10, whose scale is referred to the datum plane at 687 m a.s.l.), corresponding approximately to 20-30 m depth from topography, allows to highlight many continuous events, whose geological significance and possible interpretation are discussed in the following paragraph.

4. Comparison between SH- and P-wave seismic sections

The SH-wave and P-wave seismic sections (from Stucchi et al. (2014), redrawn in Fig. 11b) are used for combined analysis. Figure 11 displays the SH- and P-wave sections in depth and clearly evidences the differences in terms of seismic resolution. The higher resolution that can be attained with SH-waves compared to P-waves is one of the main reasons that motivate the use of the shear waves instead of compressional waves in a near surface reflection seismic survey. By using the (λ/4) criterion and trying to be conservative with regard to the value employed for SH-wave velocity (280 m/s) and frequency (30 Hz), we obtain a resolution around 2.5 m for the SH-wave section and around 9 m for the P-wave section (v=1800 m/s and f=50 Hz) at the expected shallowest slip surface (12-19 m of depth from topography,

Federici et al., 2002). This high resolution is a key-point that allows to trace the near-surface layers responsible for the shallow minor landslides that cause the major damages. The drawback of this higher resolution is the limited capacity of in-depth penetration due to increased energy absorption. In our case the energy absorption is manifested as an attenuation of the signal below 50 m, clearly evident in Fig. 11. However, by means of the SH-wave section we can better characterize the internal structure of the landslide in the investigated area and add important information to the knowledge brought in by the P-wave section at greater depths. As outlined in Stucchi et al. 2014, the P-wave seismic method is effective in locating the deepest highly deformed rocky layer, recognized as the main reflector in the P-wave seismic image of Fig. 11b (yellow area). This observation is supported by the high-amplitude and continuity of the reflection and also by its depth, which matches the top of the undisturbed bedrock. This reflector slightly deepens along the line, showing two small upward concavities. Unfortunately, no information is provided by the P-wave seismic image at shallower depth, leaving the internal structure of the geological body unresolved. On the other hand, this is the area where the SH-wave reflection seismic technique is more effective and where many continuous events are visible with good S/N ratio (Fig. 11a). The occurrence of the troughs on both P- and SH profiles (Fig. 11) at 40 m depth around CMP$_P$ 11 and the interpreted top of undisturbed bedrock on the P-wave section, suggest to use this correspondence as a possible key to extend the interpretation along the line. In this respect, the main movement layer can be interpreted on the SH section as a 5 to 10 m thick region deepening from 40 m down to 50 m (green area in Fig. 11a), and dipping in the direction of the slope. This area has also been re-drawn on the P-wave section of Fig. 11b for better comparison. The shallower layers are instead characterized by a different dipping trend, flatter or moving in opposite direction. Below the green region, reflections are less continuous and events show smaller amplitudes than above. A possibility is that most of the seismic energy does not penetrate below the weak region representing this highly deformed rocky layer, while the seismic energy above this zone succeeds in fairly well depicting the geometry of the structures characterizing the landslide (Fig. 11). A feature observed in the upper portion of the SH-wave section from 60 m to 92 m along x-coordinate (Fig. 11) is the sequence of shallow events that mimic an anticline structure. The downward concave reflectors are consistent with the contact surfaces of different bodies composed by layers of coarse material (gravel, sands) and individual rock slabs, as documented by borehole stratigraphy (Fig. 2b, see also Federici et al., 2002; Stucchi et al., 2014). These downward concave events are floored by a reflector that results evident in the entire SH-wave section at a depth variable between 15 and 20 m from topography (blue-dashed line in Fig. 11). This

basal reflector corresponds to the sliding surface of the shallow landslide detected by the movements registered in the S3 borehole (Fig. 2a, b) (Federici et al., 2002). Moreover, slightly sinuous and discontinuous events characterize the uppermost part of the SH-wave section between the 15 m and 60 m x-coordinate (Fig 11). These events stand on a continuous reflector (purple-dashed line in Fig 11) ranging between 5 and 15 m of depth from topography, that can be interpreted as the sliding surface of a landslide shallower than the above interpreted one.

Summing up, the events in the SH-wave section (Fig. 11) display a trend that is consistent with the expected geomorphological setting, and that can be interpreted as reflectors related to the deep rocky layer favouring gravitational deformation, slip surfaces and internal non-homogeneity of minor landslides that have dismantled the main complex landslide.

5. Conclusions

This work demonstrates that the high-resolution SH reflection seismic method can be used to study complex landslide bodies complementing the main geologico-geomorphological characteristics of the mass movements. The use of the SH-wave method is motivated by the higher resolution that can be attained compared to the P-waves, which is a key issue when the seismic reflection survey is used to investigate the very shallow portion of a deep-seated landslide. A careful planning of the acquisition and a dedicated processing sequence, which preserves the reflections observed at the shot level, must be designed to remove the various kinds of noise present and to obtain a migrated section with good S/N ratio. In this respect, the source and receiver acquisition parameters adopted in the current study allow the eigenvalue and fk filters to be sufficiently effective to enhance the signal against the noise, in particular the Love waves. Reflectors consistent with a deep highly-deformed rocky layer and shallower slip surfaces were imagined by the SH-wave reflection survey, so as to match with the data already available (P-wave reflection and borehole data). The results confirm that the Patigno landslide is composed by shallow complex landslides resting on a deep-seated gravitational slope deformation. Our experience confirms that a joint use of SH-wave seismic reflection providing thorough information about the shallow part of the subsurface and of P-wave seismic reflection, able to image the main discontinuity at depth, gives a more robust and reliable description of the whole landslide body. In this regard, the complete knowledge of the landslide internal setting is fundamental to plan adequate and effective defense strategies.

Finally, it is worth noting that the Patigno landslide represents a kind of destabilization phenomenon commonly affecting the Apennine slopes, i.e. deep-seated deformations or landslides reactivated by surface movements that are often the most destructive. Therefore, this work can be of interest and serve as a guide for the study and investigation of other sites with similar characteristics.

References

Aleardi, M., Tognarelli, A., Mazzotti A., 2016. Characterization of shallow marine sediments using high-resolution velocity analysis and genetic-algorithm-driven 1D elastic full-waveform inversion. Near Surface Geophysics, 14(5), 449-460. doi: 10.3997/1873-0604.2016030

Apuani, T., Arosio, D., De Finis, E., Stucchi, E., Zanzi, L., Ribolini, A., 2012. Preliminary seismic survey on the unstable slope of Madesimo (Northern Italy). 25th Symposium on the Application of Geophysics to Environmental and Engineering Problems *(SAGEEP)*, Expanded Abstracts, 452-459.

Bexfield C. E., McBride J.H., Pugin A.J.M., Ravat D., Biswas S., Nelson W.J., Larson T.H., Sargent S.L., Fillerup M.A., Tingey B.E., Wald L., Northcott M.L., South J.V., Okure M.S. , Chandler M.R., 2006. Integration of P- and SH-wave high-resolution seismic reflection and micro-gravity techniques to improve interpretation of shallow subsurface structure: New Madrid seismic zone. Tectonophysics 420, 5 – 21.

Beilecke, T., Krawczyk C. M., Ziesch J., Tanner D. C., 2016. Near-surface fault detection using high-resolution shear wave reflection seismics at the CO2CRC Otway Project site, Australia, Jourtnal of Geophysical Research, Solid Earth, 121, 6510–6532, doi:10.1002/2015JB012668.

Binbin M., Xia J., Xu Y., 2015. Finite-difference modeling of SH-wave conversions in shallow shear-wave refraction surveying. Journal of Applied Geophysics 119 71–78. http://dx.doi.org/10.1016/j.jappgeo.2015.05.009

Bichler A., Bobrowsky P., Best M., Douma M., Hunter J., Calvert T., Burns R., 2004. Three-dimensional mapping of a landslide using a multi-geophysical approach: The Quesnel Forks landslide. Landslides 1(1), 29–40.

Carvalho, J., Ghose, R., Alves, D., Leote, J., 2016, Earthquake faulting-related deformation in soil evidenced in S-wave shallow reflection data: field results from Portugal, Geophysics, vol. 81 (5), IM97-IM108. doi:10.1190/geo2015-0040.1.

Castagna, J.P, Backus M.M., 1993. Offset-Dependent Reflectivity - Theory and Practice of AVO Analysis. Society of Exploration Geophysicists, Investigations in Geophysics, 8.

Grandi, A., A. Mazzotti, E. Stucchi, 2007. Multicomponent velocity analysis with quaternions: Geophysical Prospecting, 55, 761–777, doi:10.1111/j.1365-2478.2007.00657.x.

Ghose, R., Carvalho, J., Loureiro, A., 2013, Signature of fault zone deformation in near-surface soil visible in shear-wave seismic reflections. Geophysical Research Letters, 40 (6), 1074-1078, DOI: 10.1002/grl.50241.

Guy E.D, Nolen-Hoeksema R.C., Daniels J.J., Lefchik T., 2003. High-resolution SH-wave seismic reflection investigations near a coal mine-related roadway collapse feature. Journal of Applied Geophysics. 54: 51-70. DOI: 10.1016/S0926-9851(03)00055-7

Guy, E.D., 2006. High-Resolution P- and S-wave Seismic Reflection Investigation of a Shallow Stratigraphic Sequence. Electronic Journal of Geotechnical Engineering, 11, 37 pp.

Federici, P.R., Puccinelli, A., Chelli, A., D'Amato Avanzi, G., Ribolini, A., Verani, M., 2002. The Large Landslide of Patigno (Northern Apennines, Italy): Geological, geomorphological and geognostic integrated analysis. In: Landslides, (eds J. Rybar, J. Stemberg and P. Wagner). Swets and Zeitlinger, Lisse, 547–552.

Haines S.S, Ellefsen K. J., 2010. Shear-wave seismic reflection studies of unconsolidated sediments in the near surface. Geophysics, 75, B59–B66 10.1190/1.3340969

Inazaki, T., 2004. High resolution reflection surveying at paved areas using S-wave type land streamer, Exploration Geophysics, 35, 1–6.

Neidell, N. S., M. T. Taner, 1971. Semblance and other coherency measures for multichannel data. Geophysics, 36, 482–497, doi: 10.1190/1.1440186.

Johnson W. J., Clark J. C., 1992. Improving Subsurface Resolution with the Seismic Reflection Method: Use S-waves. Ground Water Management, 11,655-663.

Jongmans, D., Garambois, S., 2007. Geophysical investigation of landslides: A review. Bulletin Société Géologique de France, 178(2), 101–112.

Krawczyk, C., U. Polom, T. Beilecke, 2013. Shear-wave reflection seismics as a valuable tool for urban applications, Leading Edge, 32(3), 256–263. doi:10.1190/tle32030256.1.

Malehmir A., Saleem M.U., Bastani M., 2013. High-resolution reflection seismic investigations of quick-clay and associated formations at a landslide scar in southwest Sweden. Journal of Applied Geophysics, 92, 84–102.

Palmer, D., 1981. An introduction to the generalized reciprocal method of seismic refraction interpretation. Geophysics, 46(11), 1508-1518.

Petronio L., Boaga J., Cassiani G., 2016. Characterization of the Vajont landslide (North-Eastern Italy) by means of reflection and surface wave seismic. https://doi.org/10.1016/j.jappgeo.2016.03.012

Polom U., Bagge M., Wadas S., Winsemann J., Brandes C., Binot F., Krawczyk C., 2013. Surveying near-surface depocentres by means of shear wave seismics. First Break, 31(8), 67–79.

Pugin, A.J.M, Larson, T., Sargent, S., McBride, J., Bexfield, C., 2004. Near-surface mapping using SH-wave and P-wave seismic land-streamer data acquisition in Illinois, U.S. The Leading Edge 23, 677–683.

Pugin, A.J.M., Sargent, S.L., Hunt, L., 2006. SH and P-wave seismic reflection using landstreamers to map shallow features and porosity characteristics in Illinois. Symposium on the Application of Geophysics to Engineering and Environmental Problems *(SAGEEP)*. Expanded Abstracts, 1094-1109.

Pugin, A.J.M., Pullan, S.E., Hunter, J.A., Oldenborger, G.A., 2009. Hydrogeological prospecting using P- and S-wave landstreamer seismic reflection methods. Near Surface Geophysics, 7, 315–327.

Pugin, A.J.M., Brewer K., Cartwright T., Pullan S., Didier P., Crow H., Hunter J., 2013. Near surface S-wave seismic reflection profiling - New approaches and insights, First Break, 31(2), 49–60. doi:10.3997/1365-2397.2013005.

Stucchi, E., Mazzotti, A., 2009. 2D seismic exploration of the Ancona landslide (Adriatic Coast, Italy). Geophysics, 74(5), B139.

Stucchi, E., Ribolini, A., Anfuso, A., 2014. High-resolution reflection seismic survey at the Patigno landslide, Northern Apennines, Italy. Near Surface Geophysics, 4, 559-571.

Tognarelli, A., Stucchi, E., Ravasio, A., Mazzotti, A., 2013. High-resolution coherency functionals for velocity analysis: An application for subbasalt seismic exploration. Geophysics, 78 (5), U53-U63, doi:10.1190/GEO2012-0544.1

Tognarelli, A., Stucchi, E., Ribolini, A., Lauriti E., Meini, L., 2015. SH-wave Seismic Reflection at the Patigno Landslide and Integration with P-wave Reflection Data. 21[St] European Meeting of Environmental and Engineering Geophysics, Turin, Extended Abstract.

Wadas S.H., Polom U., Krawczyk C.M., 2016. High-resolution shear-wave seismic reflection as a tool to image near-surface subrosion structures – a case study in Bad Frankenhausen, Germany. Solid Earth, 7, 1491–1508.

Wiyono W., Polom U., Krawczyk C.M., 2013. Comparison of high-resolution P- and SH-wave reflection seismic data in alluvial and pyroclastic deposits in Indonesia. 19th European Meeting of Environmental and Engineering Geophysics, Bochum, Extended Abstract.

Woolery E. W., Ron Street R., 2002. Quaternary Fault Reactivation in the Fluorspar Area Fault Complex of Western Kentucky: Evidence from Shallow SH-wave Reflection Profiles. Seismological Research Letters, vol. 73 no. 5 628-639. https://doi.org/10.1785/gssrl.73.5.628

Young R. A., Hoyos J., 2001. Near-Surface, SH-Wave Surveys in Unconsolidated, Alluvial Sediments. The Leading Edge, 20(9): 936–948.

Figures

Figure 1. Geographical (a) and geomorphological (b) sketch maps of the Patigno landslide. The Patigno landslide body (1); limestone with interbedding of grey-black argillites (Argille e Calcari Formation) (2); limestone-marly turbidites (Calcari del Groppo del Vescovo Formation) (3); pelitic-siltitic turbidite (Arenarie di Ponte Bratica Formation) (4); limestones and olistolithes of serpentinite (Ottone S. Stefano Unit) (5); borehole (6).

Figure 2. Seismic line position (P and SH) (a) and borehole stratigraphy (after Federici et al. 2002) (b). The position of the first and last station of the SH-wave survey is reported. Landslide material (boulders, gravel, sand) (1); densely fractured rocks (argillites and limestone) (2); undisturbed bedrock (argillites and limestone) (3).

Figure 3. Layout of the acquisition scheme. The small yellow triangles indicate the receivers, while the red dots indicate the source location. To help understand the acquisition procedure we used, the station number is also shown in blue. The source-receiver pattern is moved 6 times along the line in downhill direction, yielding a total profile length of 86.25 m and 116 stations with 0.75 m spacing.

Figure 4. a) and b) Raw shot gathers acquired in the same location with NE-SW and SW-NE polarization respectively; c) Shot resulting from vertical and polarity reversal stacking.

Figure 5. Flowchart of the processing sequence. As reported in the legend, the processing steps applied in shot domain, in cdp domain and post-stack are highlighted in yellow, orange and green, respectively. Where appropriate, the most important processing parameters are also indicated.

Figure 6. Outcome of the denoising procedure performed in the shot domain, whose main objective is to attenuate the Love waves. A raw shot gather is shown in a) following the vertical stacking and reversal summation. The other frames display the same shot gather after the application of: b) eigenvalue filter (4 eigenimages are subtracted); c) *f-k* polygonal filter and d) time variant (inverse of the envelope) gain.

Figure 7. Refraction model obtained by the Generalized Reciprocal Method (GRM, Palmer 1981) applied to compute the refraction statics on a two-layer model. The velocity of the upper layer, determined by fitting the first breaks of the shortest offset traces, has a value of $V_0 \approx 150$ m/s. The refractor offset that we used ranges from 9 m to 18 m and the estimated refractor velocity varies between 175 m/s and 240 m/s. The final datum was set at 687 m a.s.l..

Figure 8. Example of a CMP supergather (a) and the related velocity spectra (b, c) used to pick the velocity model b) and c) show the spectra computed by the semblance functional (C_S) and by the complex matched functional (C_{CM}) respectively. Evident from both panels is the higher resolution of the complex matched functional (C_{CM}) compared with the classical semblance (C_S). (The color scales are different on account of the different values resulting from the two algorithms used; however, in both panels, they are set to the best trade off between relative maxima highlight and resolution). The white dots in frame b) and c) are the picked values for the specific gather. The arrows indicate the t_0 ,V_{SH} pairs corresponding to the hyperbola drawn with red dashed lines in Fig.8a).

Figure 9. a) Stack section after the time variant band-pass filter and b) the same section with the time variant filter and the *f-x* deconvolution applied. The parameters used are indicated in the flowchart of Fig. 5. As can be observed, the effect of the *f-x* deconvolution is to remove some residual noise in the upper part of the section, thus making the continuity of the events clearer. The red dots in frame b) indicate the t_0 times of the reflection events picked in Fig. 8a.

Figure 10. Final Kirchhoff depth migrated SH-wave seismic section over-imposed to the velocity field used for migration. The section is referred to the datum at 687 m a.s.l.. Many reflectors with good S/N ratio are observed down to 20-30 m from topography (40 m on the vertical scale), while at greater depths only some faint events can be recognized with a trend and signature different from that of the shallower ones.

Figure 11. Comparison of the SH- and P-wave seismic sections (a and b respectively) both referred to the datum plane at 687 m a.s.l.. Note the higher resolution that can be attained with the SH-wave survey compared to the P-wave survey. On the SH-wave seismic section (a) the region highlighted in green is related to the main slip surface separating the upper part of the section characterized by many reflectors from the lower one in which the reflected

energy is low. Two reflectors interpreted as sliding surfaces of the shallow landslide are indicated with purple and blue dashed lines. The yellow area in the P-wave seismic section (b) shows the region interpreted as the main slip surface from the P-wave data alone (Stucchi et al., 2014). The satisfactory match between the SH- and P-wave outcomes supports the interpretation of the shallower reflectors as related to small reactivation slip surfaces delineating shallower and minor landslides (blue and purple dashed lines).

Figure 1

a) SH-Waves
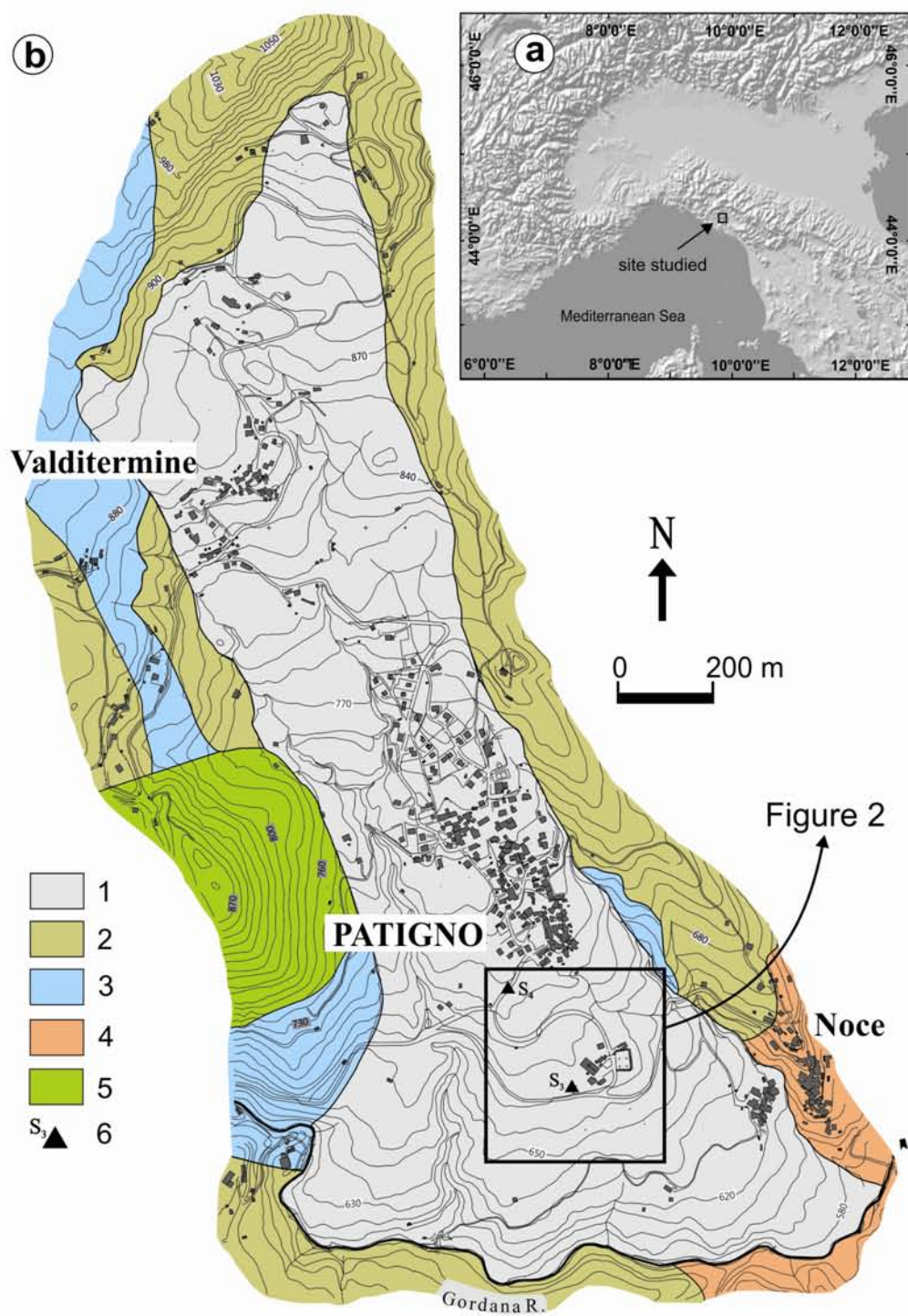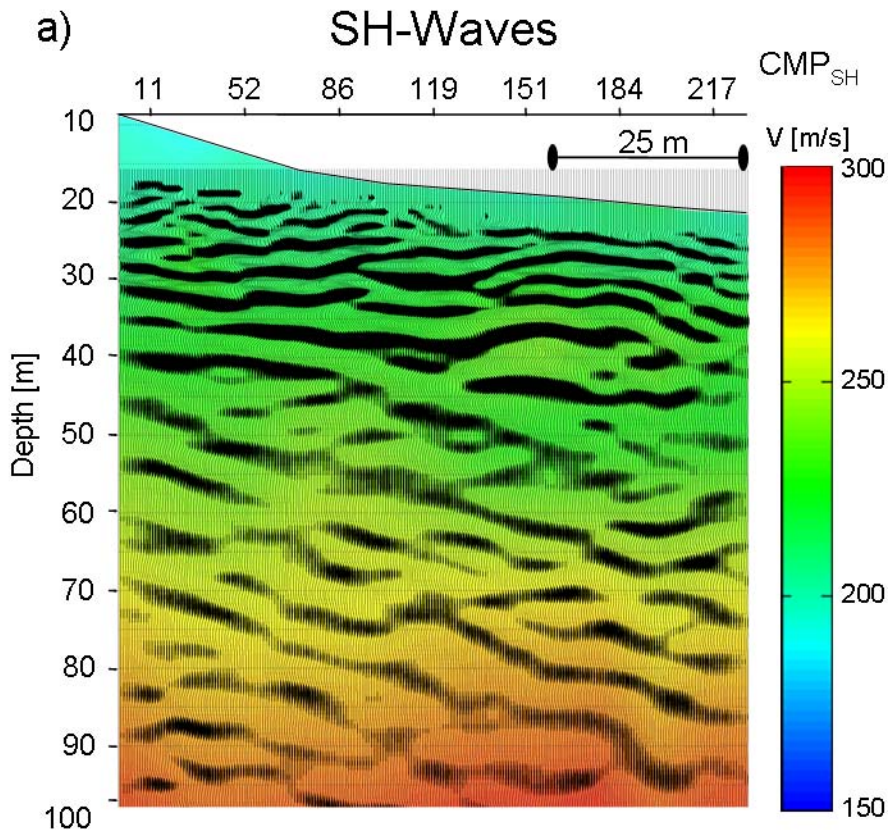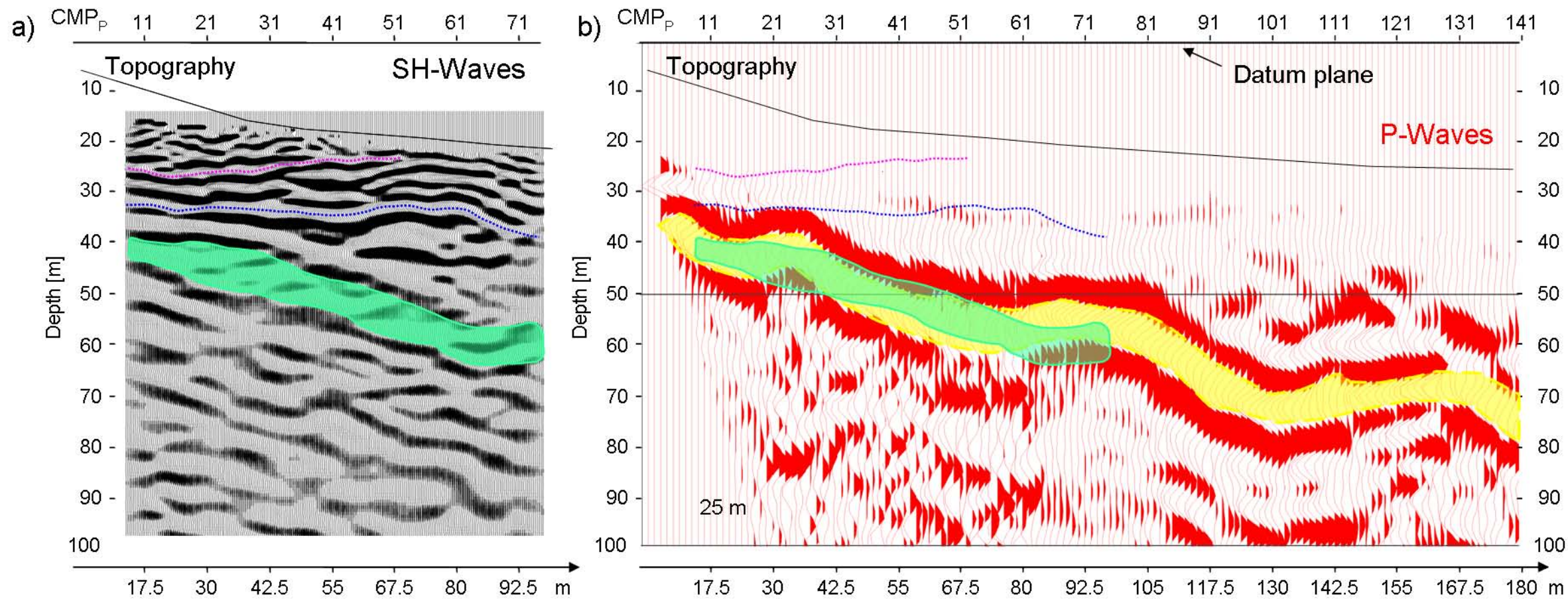
Figure 10

Figure 11

Figure 2
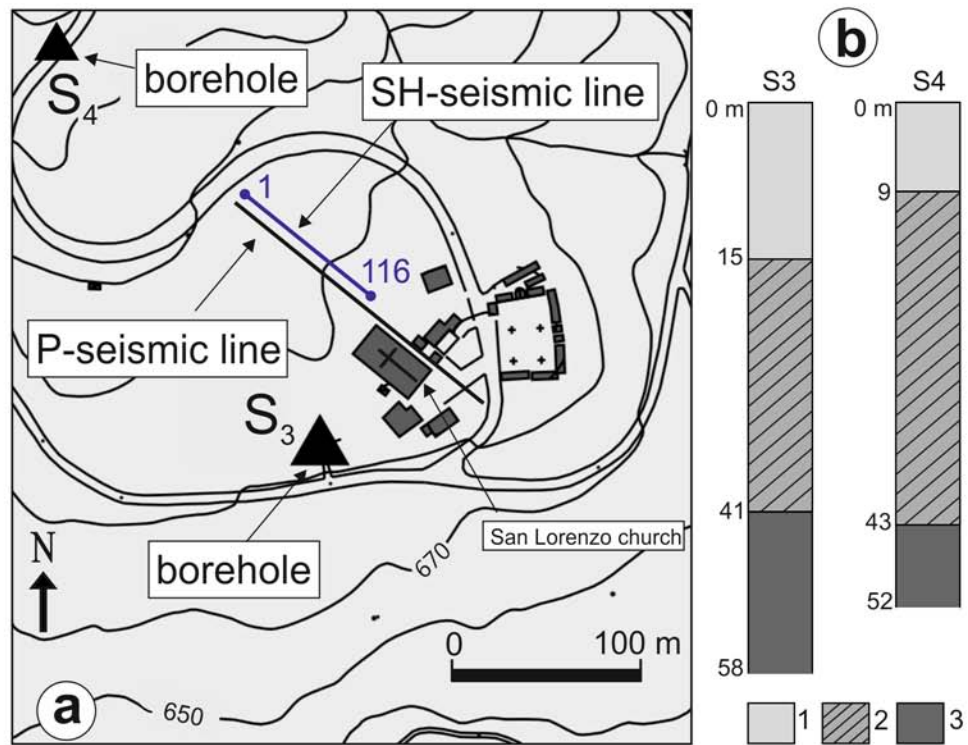
Figure 3

ACQUISITION SCHEME

Figure 4

a) NE-SW

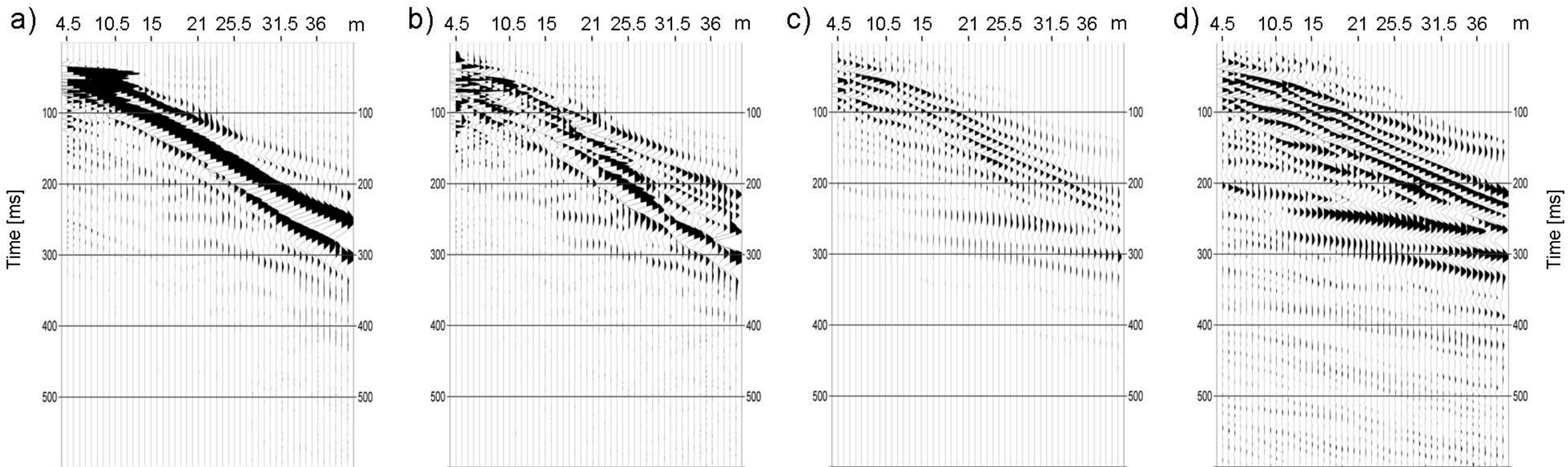b) SW-NE

c) stacked shot
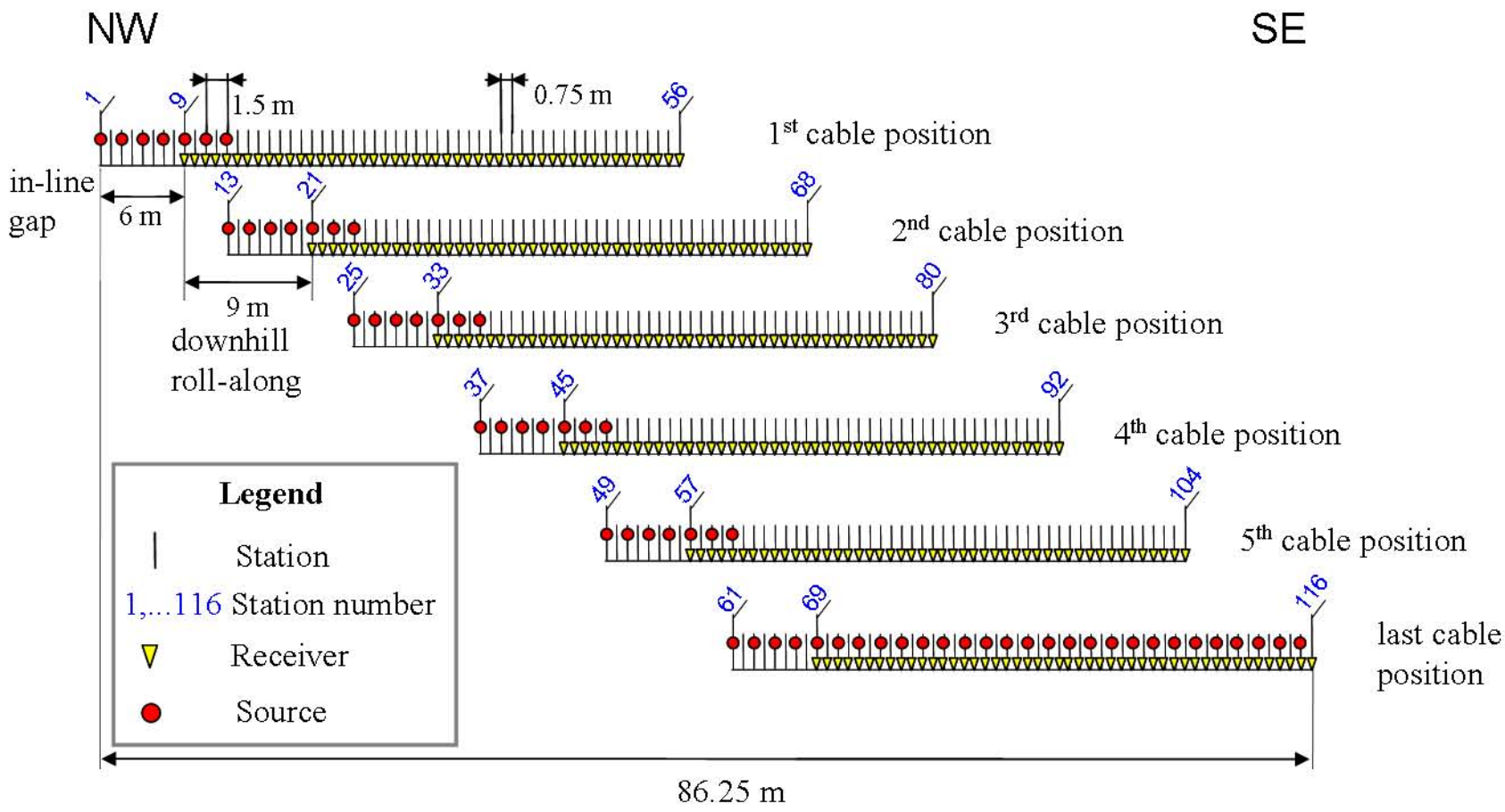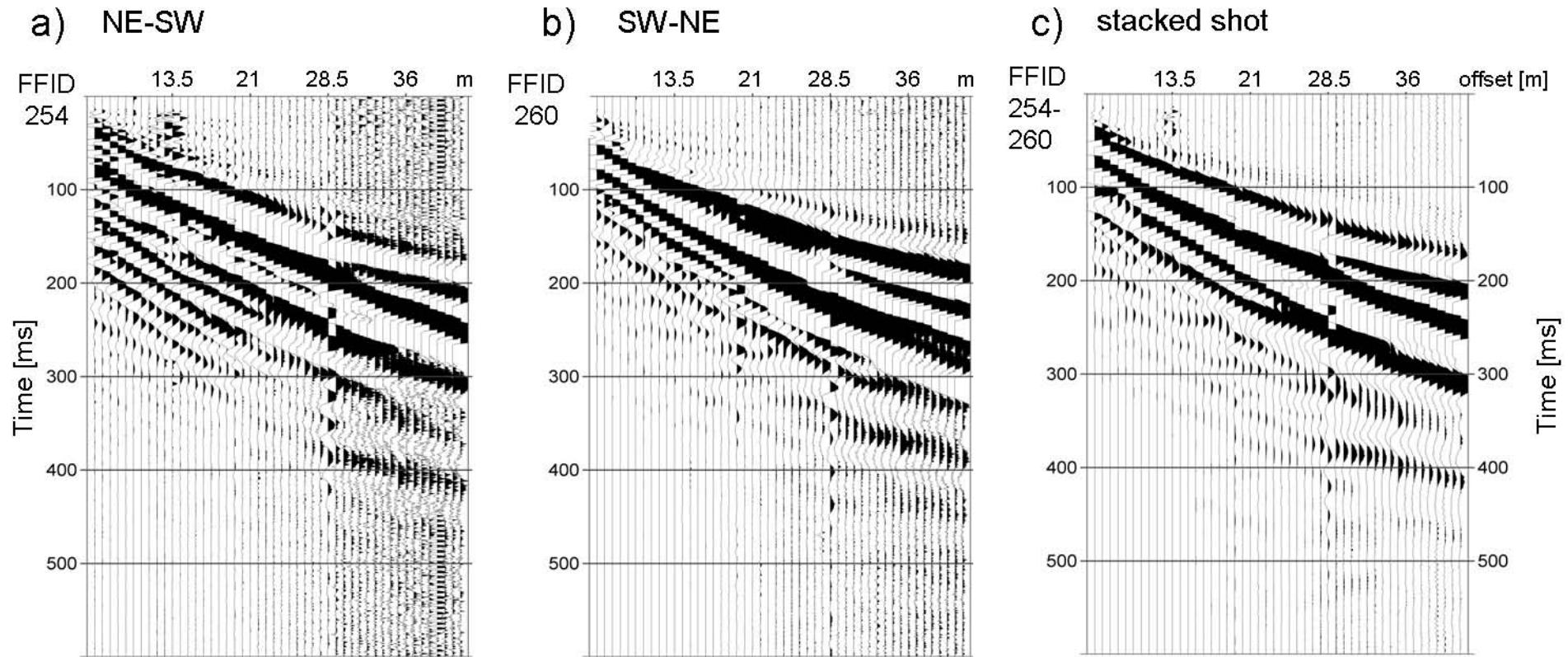
Figure 5

Figure 6

Figure 7

SH-Wave Refraction Model
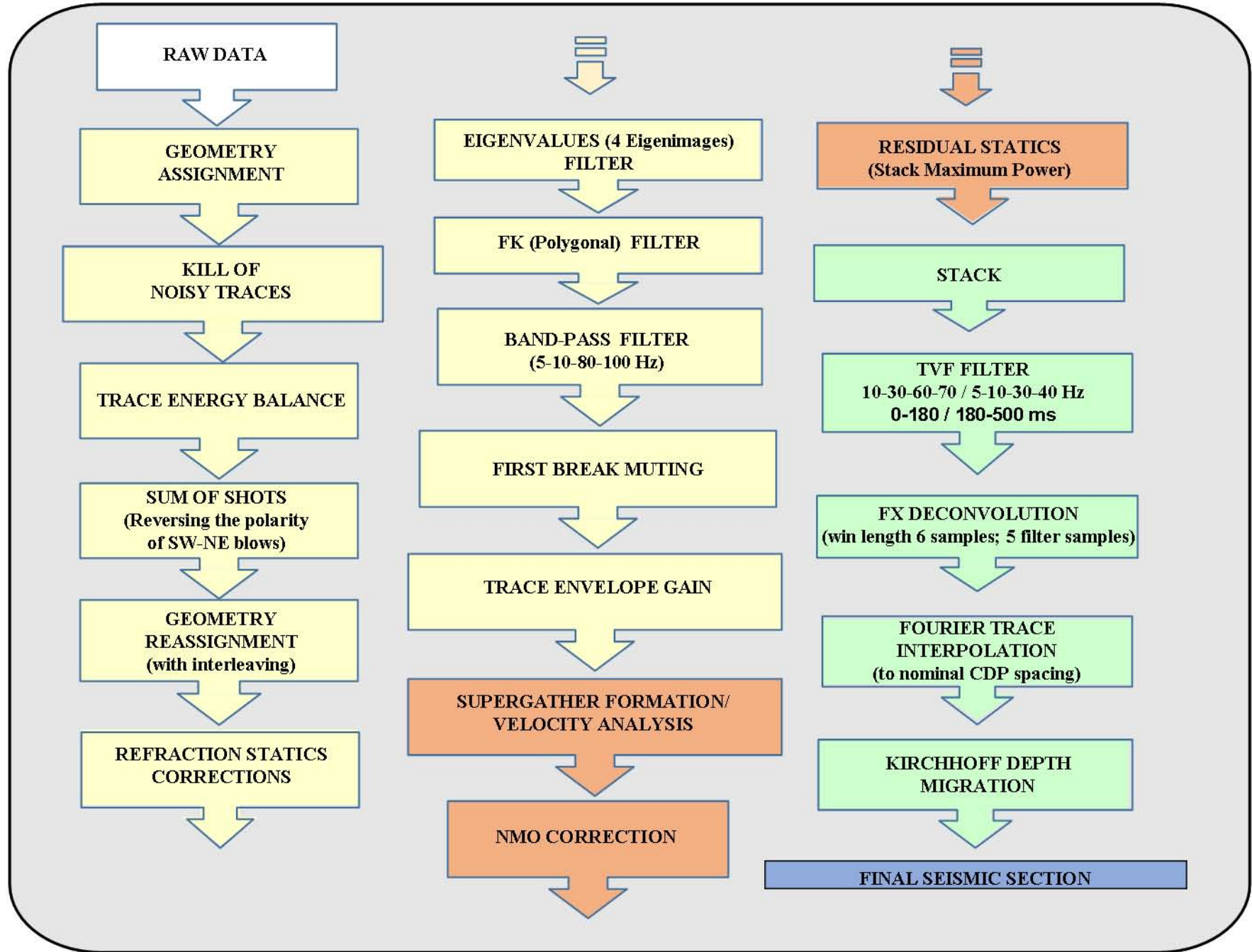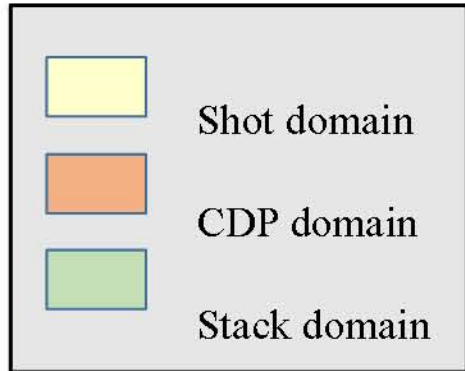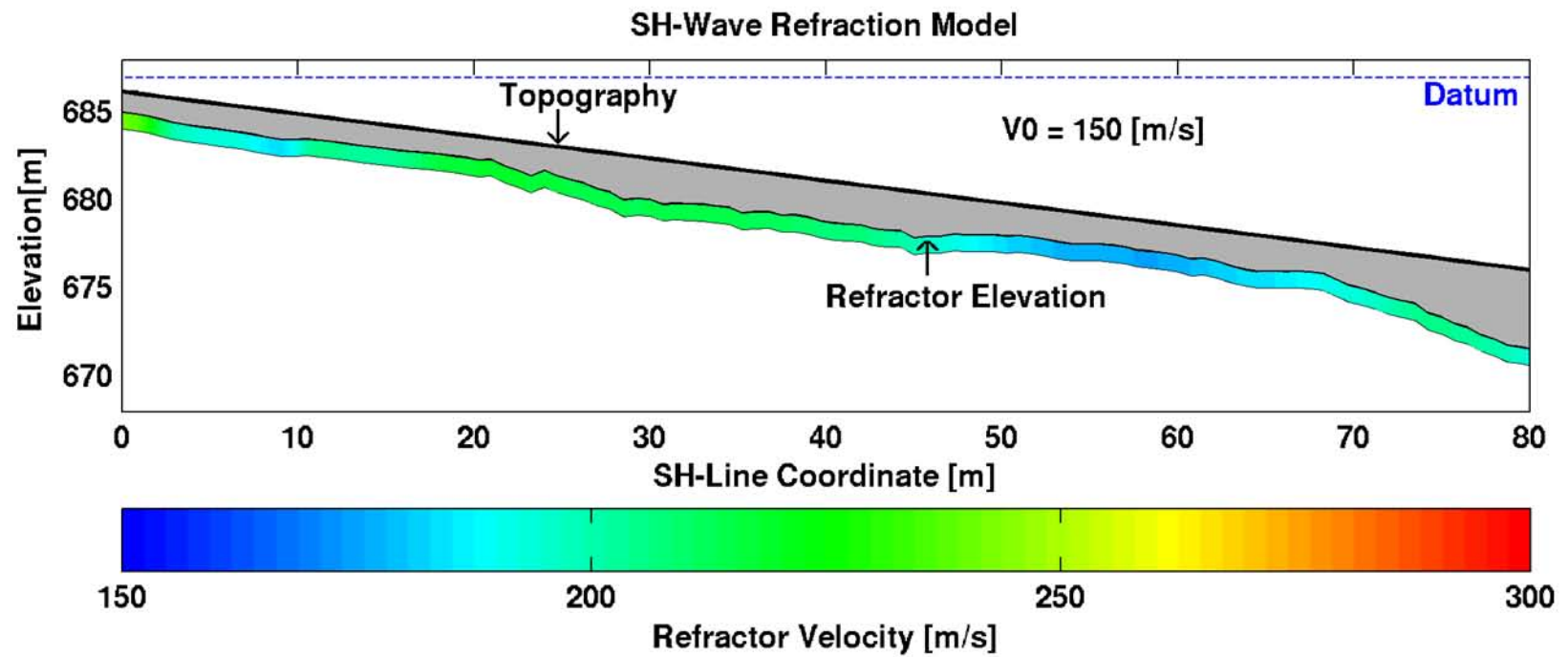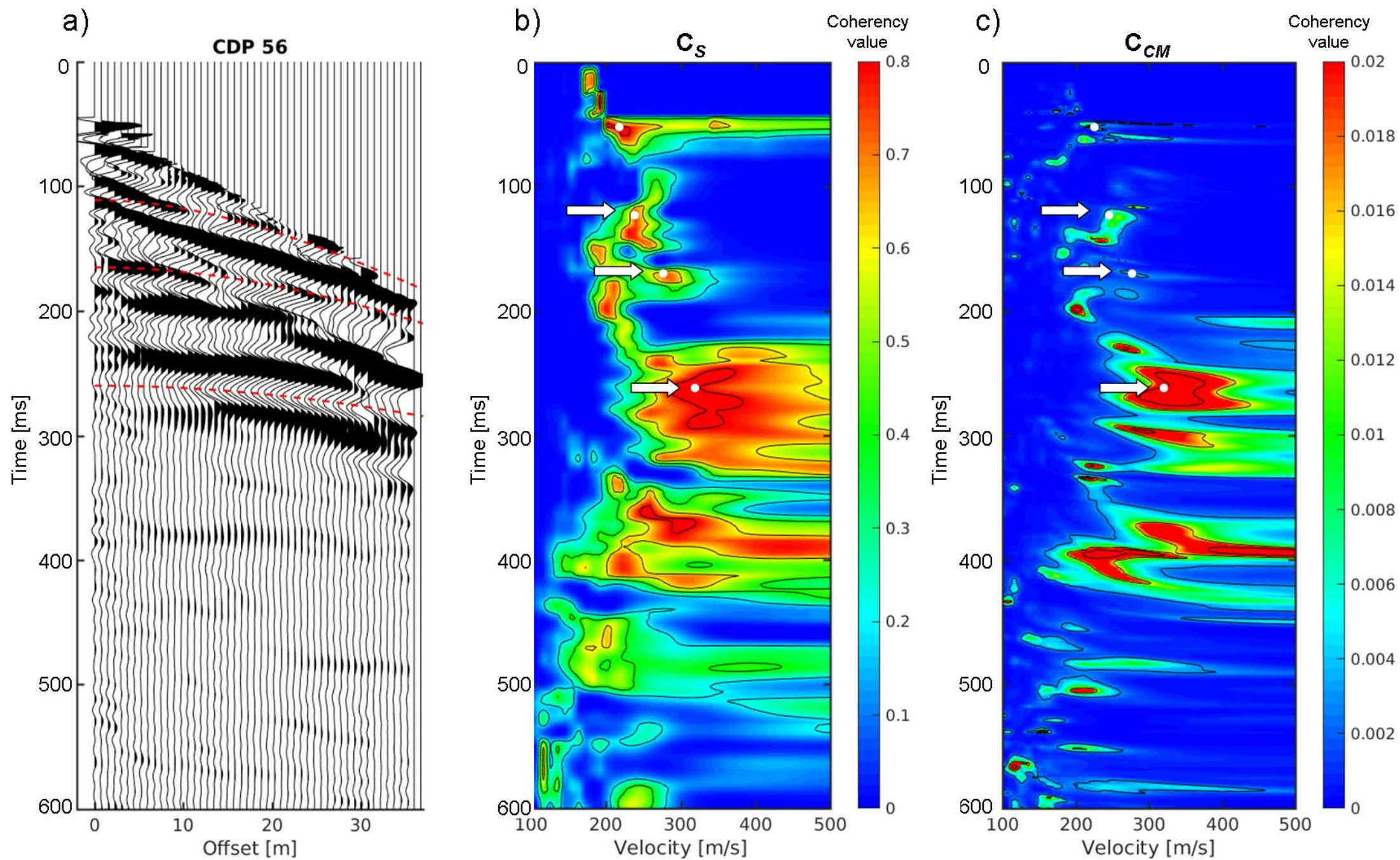
Figure 8

Figure 9
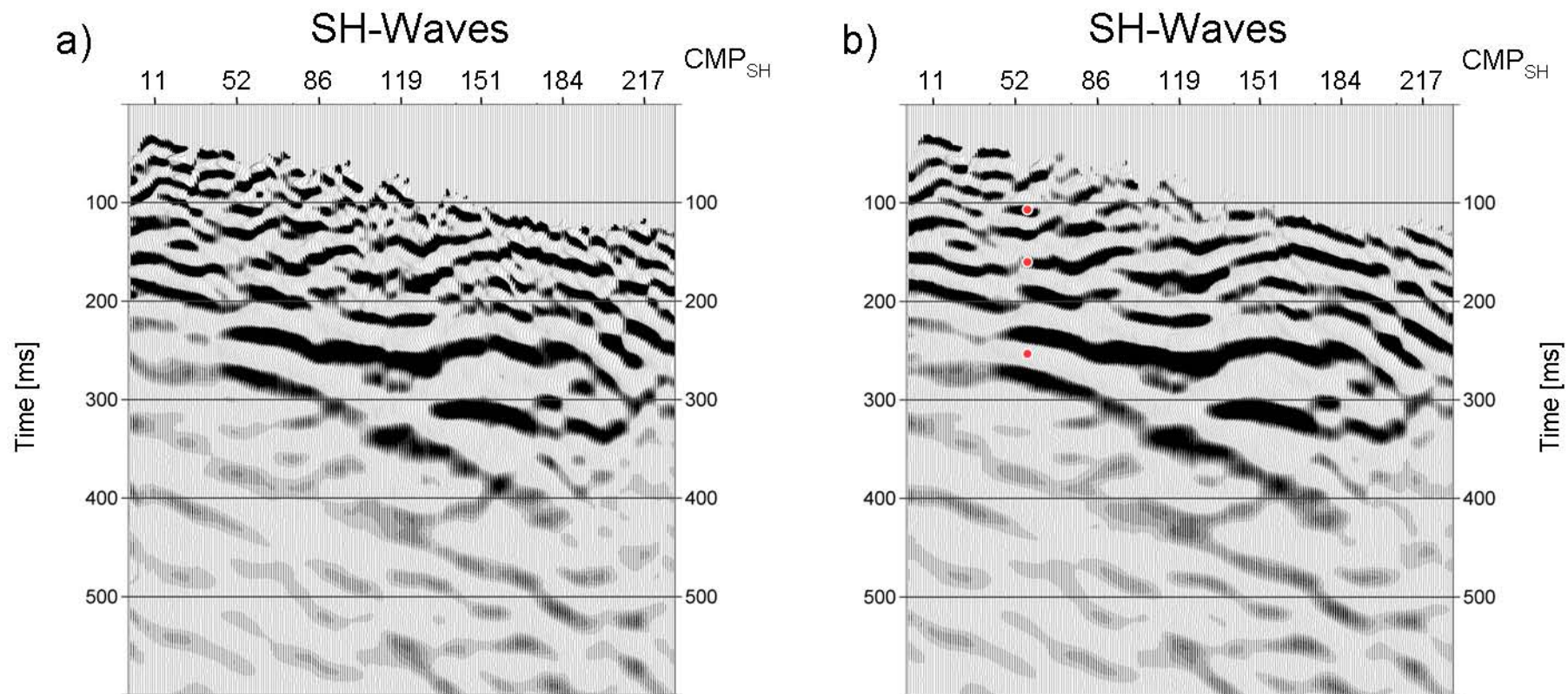
Table 1

ACQUISITION PARAMETERS	
Number of receivers	48
Total number of blows	763
Total number of sources	63
Total length of the line	86.25 m
Number of spread position	6
Minimum offset	0 m
Maximum offset	41.25 m
Source interval	1.5 m
Receiver interval	0.75 m
Maximum fold	24°
Final datum	687 m
Sample rate	0.5 ms
Recording length	1 s